RESEARCH ARTICLE

Key Points:
- New vector-based one-line model for evolution of sandy coasts developed
- Wave climate variability is important in controlling equilibrium form of bays
- The characteristic response time of a crenulate bay scales diffusively with bay size

Correspondence to:
M. D. Hurst,
mhurst@bgs.ac.uk

Exploring the sensitivities of crenulate bay shorelines to wave climates using a new vector-based one-line model

Martin D. Hurst[1], Andrew Barkwith[1], Michael A. Ellis[1], Chris W. Thomas[1], and A. Brad Murray[2]

[1]British Geological Survey, Nottingham, UK, [2]Duke University, Durham, North Carolina, USA

Abstract We use a new exploratory model that simulates the evolution of sandy coastlines over decadal to centennial timescales to examine the behavior of crenulate-shaped bays forced by differing directional wave climates. The model represents the coastline as a vector in a Cartesian reference frame, and the shoreface evolves relative to its local orientation, allowing simulation of coasts with high planform-curvature. Shoreline change is driven by gradients in alongshore transport following newly developed algorithms that facilitate dealing with high planform-curvature coastlines. We simulated the evolution of bays from a straight coast between two fixed headlands with no external sediment inputs to an equilibrium condition (zero net alongshore sediment flux) under an ensemble of directional wave climate conditions. We find that planform bay relief increases with obliquity of the mean wave direction, and decreases with the spread of wave directions. Varying bay size over 2 orders of magnitude (0.1–16 km), the model predicts bay shape to be independent of bay size. The time taken for modeled bays to attain equilibrium was found to scale with the square of the distance between headlands, so that, all else being equal, small bays are likely to respond to and recover from perturbations more rapidly (over just a few years) compared to large bays (hundreds of years). Empirical expressions predicting bay shape may be misleading if used to predict their behavior over planning timescales.

1. Introduction

In this contribution we explore how wave conditions influence the morphology of embayed beaches using a new one-line model for coastline evolution. One-line models are coastal evolution models in which the coast is represented by a single line. They are built around a central assumption that the cross-shore beach profile maintains some average morphology, which is only temporarily perturbed by storm events [cf. *Masselink et al.*, 2015], and therefore, a single shoreline contour is sufficient to describe the planform morphology of the coast.

The curved planform morphology of embayed beaches can be observed at various length-scales at coastlines, from a few hundred meters to several kilometers (Figure 1). These log spiral-shaped [*LeBlond*, 1972], crenulate-shaped [*Silvester and Ho*, 1972], hook-shaped [*Rea and Komar*, 1975], or zeta-shaped [*Zenkovich*, 1967] bays occur in the lee of headlands or man-made coastal structures where erosion and/or littoral drift is inhibited in the face of a dominant direction of wave incidence [*Yasso*, 1965]. A highly concave portion of shoreline forms on the downdrift side of the headland where the coastline is shadowed from the dominant wave direction and subject to waves that diffract around the headland [e.g., *Yasso*, 1965; *LeBlond*, 1972; *Rea and Komar*, 1975; *Hsu et al.*, 2010].

Embayed beaches tend toward an equilibrium form under a prevailing wave climate. The planform morphology will adjust until gradients in alongshore sediment flux are minimized (net alongshore sediment flux is constant). Alongshore sediment flux will be negligible on an equilibrium coastline when there are no external sediment inputs [*Tanner*, 1958; *LeBlond*, 1979; *Komar*, 1998; *Hsu et al.*, 2010]. Subsequent changes in planform morphology may occur such as beach rotation, driven by changes in wave climate characteristics that alter alongshore [e.g., *Turki et al.*, 2013; *Ratliff and Murray*, 2014] or cross-shore [e.g., *Harley et al.*, 2011] sediment transport.

One-line models of shoreline evolution can reproduce embayed beach morphology in the lee of a headland or promontory [*LeBlond*, 1972; *Rea and Komar*, 1975; *Hanson*, 1989; *Littlewood et al.*, 2007; *Iglesias et al.*, 2009; *Weesakul et al.*, 2010; *Barkwith et al.*, 2014a, 2014b]. *Rea and Komar* [1975] used simple rules to describe the adjustment in wave height and direction due to diffraction in the shadow of a promontory and demonstrated
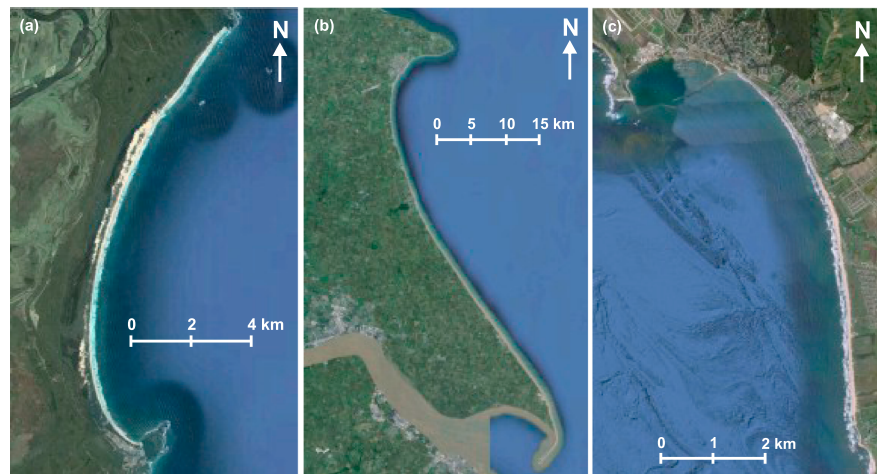
Figure 1. Examples of crenulated bay shapes at different scales. (a) Hathead Bay, Eastern Australia. (b) Flamborough Head and the Holderness Coastline, East Yorkshire, UK. (c) Half Moon Bay, California, USA.

that the resulting bay forms were similar in form to a logarithmic spiral. *Weesakul et al.* [2010] presented a similar model that found good agreement when compared to experimental data and the empirical parabolic model for bay morphology [*Hsu and Evans*, 1989]. Both of these studies examined the formation of bays under the influence of a single dominant wave direction, with the morphology of the highly curved portion of the bay controlled by diffraction of waves into the shadowed region. The study by *Littlewood et al.* [2007] neglected wave diffraction in the shadow zone yet demonstrated that a crenulate-shaped bay can still develop when there is variation in the approaching wave angles. Sediment transport in the shadow of the dominant wave direction only occurs when waves approach from the leeside of the crenulate bay. *Daly et al.* [2014] explored the sensitivity of embayment morphology to variation in wave climate using the Delft3D hydrodynamic and morphodynamic model. Starting with an idealized straight coastline between two coastal structures, the model was evolved long enough for a stable bathymetric condition to emerge. The simulations demonstrated that variation in wave approach angles exerts a significant control on bay morphology and that wave diffraction in the shadow of coastal structures or headlands is only an important control on bay morphology when the spread of wave approach angles are narrow and strongly oblique to the bay orientation.

Empirical models have been derived to approximate the shape of crenulate bay beaches, including the logarithmic spiral [*Krumbein*, 1944; *Yasso*, 1965] and the parabolic bay [*Hsu and Evans*, 1989] described further below. The parabolic model applies specifically to predicting the static equilibrium form of a bay beach behind a specified diffraction point given a predominant wave direction. *Oliveira and Barreiro* [2010] fitted these models to 42 bay beaches along the Portuguese coast in order to assess whether the beaches were stable and had reached static equilibrium. The authors found that both the logarithmic spiral and parabolic bay equations provided good fits to observed beach planforms. Fitted parabolic bay equations were consistent with these beaches being in static equilibrium, despite empirical evidence that some bays are open systems and therefore may have attained dynamic equilibrium [*Hsu et al.*, 2010]. The logarithmic spiral performed well in the curved region in the lee of an adjacent headland but cannot fit straight sections of coastline.

The logarithmic spiral was first observed to be a good fit to the planform geometry of Half Moon Bay, California, USA, by *Krumbein* [1944] (Figure 1c). The logarithmic spiral empirical model is in polar coordinates and takes the following form:

$$r = r_0 \, e^{\psi \cot \lambda} \qquad (1)$$

where r [L] is the radius from the beach to the center of the spiral, r_0 [L] is the minimum value for r, ψ [°] is the angle around the spiral (between r and r_0), and λ [°] is the spiral angle (i.e., the constant angle to the tangent of the spiral). Dimensions are given as [M]ass, [L]ength, [T]ime, and angles [°] throughout (see the notation section). The origin does not necessarily coincide with the point of diffraction [e.g., *Yasso*, 1965; *Hsu et al.*, 2010] nor does it include factors to account for, or indicate, the dominant wave conditions. The log spiral model applies only to the shadow zone [*Oliveira and Barreiro*, 2010] and is not limited to equilibrium bay shapes.

Hsu et al. [2010] were critical of this model because the diffraction point (i.e., the headland) is not specified. The coordinate origin is not required to coincide with the headland tip which is the point of diffraction, and the method does not take into account beach stability, nor does it provide an explicit relationship to incoming waves [*Hsu et al.*, 2010].

The parabolic bay equation developed by *Hsu and Evans* [1989] predicts the static equilibrium planform of a beach in relation to a specific control point (headland) in the face of particular dominant wave conditions. The expression takes the form of a second-order polynomial:

$$R = R_0 \left(C_1 + C_2(\kappa/\psi) + C_3(\kappa/\psi)^2 \right) \qquad (2)$$

C_1, C_2, and C_3 (dimensionless) are empirical coefficients [see *Hsu and Evans*, 1989], κ [°] is the angle between incoming dominant wave crests and the reference line R_0 [L] which describes the line to a downcoast reference point beyond which the shoreline is linear. R [L] is the distance to the shoreline at radial angle ψ [°] to the control line.

The ability to predict the final form of the beach has applications in understanding the future distribution and timescales over which coastal erosion will occur, or in planning for the influence of coastal interventions on downdrift coastal morphology. Indeed the induction of a crenulate bay morphology may itself be a successful strategy for stabilizing a coastline [*González and Medina*, 2001; *González et al.*, 2010; *Hardaway and Gunn*, 2010]. Yet these empirical expressions are decoupled from the physical processes that drive bay formation and evolution.

Exploratory numerical models provide a means to test the predictions of these empirical relationships. *Daly et al.* [2014] apply the Delft3D model to a bay formed between two fixed structures just ~150 m apart over a 3 year time period. Even at these scales, the authors note that the computational time required to carry out multiple simulations can be "discouraging," despite the use of a morphological acceleration factor to reduce computation time. Empirical models for bay morphology assume that the bay has achieved equilibrium, yet little is known about how long it takes for bays to attain equilibrium and what controls this response time. *Daly et al.* [2015] found that the progression to equilibrium from an initially straight coast between two headlands could be well described by an exponential function, with a rapid initial response increasing bay size, and the rate of change in bay size declining through time. However, for large bays (600 m headland separation) they were not able to run simulations long enough for equilibrium conditions to emerge. Exploratory, behavioral modeling such as the use of one-line models facilitates predicting coastal evolution at larger spatial and temporal scales (mesoscales, kilometers—tens of kilometers, tens to thousands of years) [*Murray*, 2007; *Larsen et al.*, 2014]. In this study we took a systematic approach in seeking to understand the influence of wave climate and wave transformation on the development of large embayments toward an equilibrium form. We also investigated the influence of spatial scale on the timescale to attain equilibrium. We show that coastal morphology is sensitive to both dominant wave direction and the spread of wave directions impinging the coastline and that the timescale to attain equilibrium scales diffusively with the length of separation between headlands. To do so, we developed a Coastal One-line Vector Evolution (COVE) model that simulates the evolution of high planform-curvature coastlines.

2. One-Line Coastal Evolution Models

One-line coastal models make a number of simplifying assumptions in order to conceptualize the coast. First, short-term variations due to storms or rip currents, which tend to act in the cross-shore direction [e.g., *Masselink et al.*, 2015], are considered as temporary perturbations to the long-term trend of coastal change, causing fluctuations in shoreline position. As such the beach profile is assumed to maintain a constant time-averaged form, implying that depth contours are shore-parallel [cf. *van den Berg et al.*, 2012; *Kaergaard and Fredsoe*, 2013a]. Alongshore sediment transport occurs primarily in the surf zone, and it is assumed that cross-shore sediment transport acts to maintain the equilibrium shoreface as it advances or retreats. Finally, it is assumed that alongshore sediment transport is driven by the delivery of energy to the surf zone, parameterized by the height and angle of incidence of breaking waves [*Longuet-Higgins*, 1970; *Komar and Inman*, 1970]. Waves that impinge obliquely on the coastline will cause downdrift transport, and a variety of formulations are available to describe the relationship between wave conditions and the magnitude of alongshore sediment flux [e.g., *U.S. Army Corps of Engineers (USACE)*, 1984; *Bailard*, 1984; *Deigaard et al.*, 1986; *Kamphuis*, 1991; *Soulsby and Damgaard*, 2005; *Bayram et al.*, 2007]. One-line modeling of the evolution of sandy and

"soft sediment" coastlines has proved an excellent exploratory tool to examine the dynamics of coastline evolution at mesoscales [e.g., *Pelnard-Considere*, 1956; *Hanson*, 1989; *Falqués*, 2003; *Ashton and Murray*, 2006a; *Weesakul et al.*, 2010; *Limber and Murray*, 2011; *van den Berg et al.*, 2012; *Kaergaard and Fredsoe*, 2013a].

Alongshore transport is predicted to be maximized when offshore waves (waves at the seaward limit of the shoreface) approach the coastline from an angle of ∼45° relative to the coastline orientation. The peak in the magnitude of alongshore transport with approaching wave angle leads to shoreline instability when wave approach angles are high, allowing shoreline perturbations to grow as sand waves or even spits, while low-angle wave approach drives diffuse behavior [e.g., *Ashton et al.*, 2001; *Ashton and Murray*, 2006a, 2006b; *Falqués and Calvete*, 2005; *van den Berg et al.*, 2012; *Kaergaard and Fredsoe*, 2013b]. The nature of this high-angle wave instability (HAWI) is dependent on how nearshore bathymetry is treated within the models, which modifies wave transformation to breaking. *Ashton and Murray* [2006a] assumed shore-parallel contours extend down to the shoreface depth, which results in strong HAWI facilitating the formation of flying spits, cusps and sand waves that grow continuously through time. *Falqués and Calvete* [2005] relaxed the assumption of shore-parallel contours, instead using contours that parallel the local shoreline in shallow depths, grading smoothly offshore into contours that parallel the global coastline trend. They found that HAWI was reduced when shoreline perturbations only modify contours near the coastline. *van den Berg et al.* [2012] extended the model of *Falqués and Calvete* [2005] to a quasi 2-D morphodynamic model which includes cross-shore dynamics and showed that cross-shore sediment transport is important for HAWI with more efficient cross-shore transport leading to higher instability and more rapid growth of shoreline sand waves. This suggests that counterintuitively, the assumption of an equilibrium cross-shore profile may be the optimal condition for the occurrence of HAWI in coastline evolution models, effectively requiring efficient (instantaneous) cross-shore sediment redistribution.

Until recently, most one-line models for coastal evolution have worked with relatively straight sections of coastline in which the coastline evolves perpendicular to the regional trend of the coastline. The coastline is composed of rectilinear cells [*Pelnard-Considere*, 1956; *Hanson*, 1989]. Such an approach is not capable of handling coastlines with variable orientation without violating the principal model assumptions. *Rea and Komar* [1975] circumvented this problem by using two-cell arrays oriented perpendicular to one another to allow the coastline to evolve in either the *x* or *y* direction, demonstrating that such a model could predict the formation of crenulate-shaped bays. This framework has persisted with the GENESIS model [*Hanson*, 1989] and cellular Coastal Evolution Model of *Ashton and Murray* [2006a, 2006b]. This results in mass conservation difficulties when transporting material between cells oriented in *x* and *y* since the area in between is not accounted for. Cellular one-line formulations of recurved coastlines become difficult to manage computationally, since a particular alongshore position may have multiple coastline intersections in the cross-shore direction, as shown in the schematic model diagram in Figure 2a. Where two sections of coastline might face each other, their associated shorefaces might intersect. *Weesakul et al.* [2010] successfully applied a polar coordinate system to model the high-curvature section of crenulate-shaped bays forming downdrift of a seawall or headland and the traditional one-line approach to model the rest of the coastline. However, for more generic coastline modeling it would be nontrivial to seed and abandon radial coordinate systems in the appropriate places as the model evolves.

An alternative approach uses an innovative method to coastline modeling with local coordinate systems [*LeBlond*, 1972]. A local coordinate system dictates that the shoreline evolves perpendicular to its local orientation and as such different parts of the coast can evolve in different directions, unlike in the Cartesian framework. For example, a local coordinate method is used in the MIKE21 software suite [*Kaergaard and Fredsoe*, 2013a, 2013b, 2013c]. The coastline is represented as a series of nodes, and an idealized shoreface profile is projected seaward in order to generate a bathymetry. Offshore wave conditions can then be transformed across this bathymetry in order to give breaking wave conditions that drive alongshore sediment transport. However, as noted by *LeBlond* [1972] and subsequently by *Kaergaard and Fredsoe* [2013a], if shoreline cells are considered rectangular, extending orthogonally offshore, use of a local coordinate system will violate the principle of mass conservation when the shoreline is convex or concave. Shoreface cells overlap at concave shorelines and diverge so that there are areas of the shoreface unaccounted for at convex shorelines (Figure 2b). *Kaergaard and Fredsoe* [2013a] used generated polygonal cells to circumvent this problem, but still required an iterative scheme to correct for mass balance errors when the modeled shoreface retreated or prograded.
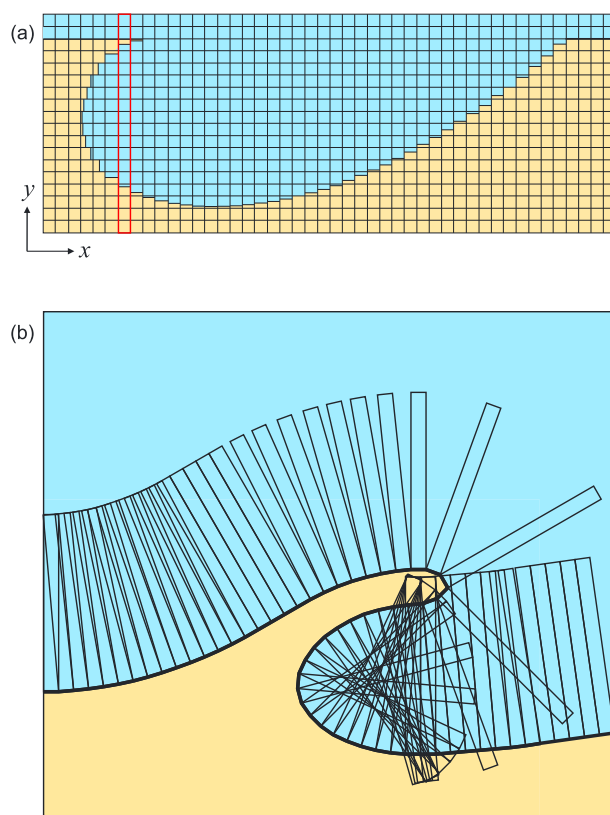
Figure 2. Schematic model domains for one-line model of coastlines with high planform-curvature. (a) Crenulate-shaped bay following a cell-based approach. Red cells highlight locations where the coastline has multiple positions in the y direction for the same x coordinate. (b) A flying spit in a local coordinate system in which rectilinear cells would result in gaps at convex seaward locations (e.g., spit tip) and overlapping cells at concave-seaward shorelines.

The COVE model, presented below, conserves mass while still allowing high planform-curvature shorelines to be modeled, using a novel conceptualization of coastal geometry and solution scheme. We demonstrate the model through application to the evolution of embayed beaches proximal to fixed headlands, similar to *Weesakul et al.* [2010], in order to explore the influence of a variable wave climate on predicted bay morphology and stability at a range of spatial scales. We compare model predictions to empirical formulae commonly used to predict equilibrium bay morphology to test their ability to predict bay form.

Documentation and source code for COVE can be found at http://mdhurst1.github.io/COVE/index.html.

3. The COVE Model

The approach we have taken in the development of COVE differs from previous similar models in that it is not restricted to a Cartesian reference frame [e.g., *Hanson*, 1989; *Falqués*, 2003; *Ashton and Murray*, 2006a]. The governing mass balance equation for the evolution of the shoreline position η [L] through time t [T] under a local coordinate system [e.g., *LeBlond*, 1972; *Kaergaard and Fredsoe*, 2013a] is a function of the divergence of alongshore sediment transport Q_{ls} [L³T⁻¹] in the alongshore direction s [L]:

$$\frac{d\eta}{dt} = f\left(\frac{dQ_{ls}}{ds}\right)$$

(3)

3.1. Alongshore Transport

Various expressions for alongshore sediment have been proposed and tested [see *Mil-Homens et al.*, 2013 and *Van Wellen et al.*, 2000, for reviews]. In particular, the Coastal Engineering Research Center (CERC) equation [*Komar and Inman*, 1970; *USACE*, 1984] is commonly implemented in one-line coastal models [e.g., *Hanson*, 1989; *Ashton et al.*, 2001; *Ashton and Murray*, 2006a; *van den Berg et al.*, 2012], in which the depth-integrated alongshore volumetric sediment transport is a function of breaking wave height H_b [L] and angle α_b [°]:

$$Q_{ls} = K_{ls} H_b^{5/2} \sin 2\alpha_b$$

(4)

where K_{ls} [L⁰·⁵ T⁻¹] is a transport coefficient. For details of how breaking waves conditions are calculated, see section 4 and Appendix A. For the transport of quartz density sand-sized material $K_{ls} = 0.4$ is used [*Komar*, 1998] but reported values vary widely [cf. *Pilkey et al.*, 2002]. This equation describes the immersive weight transport of sand (i.e., sand transport in suspension).
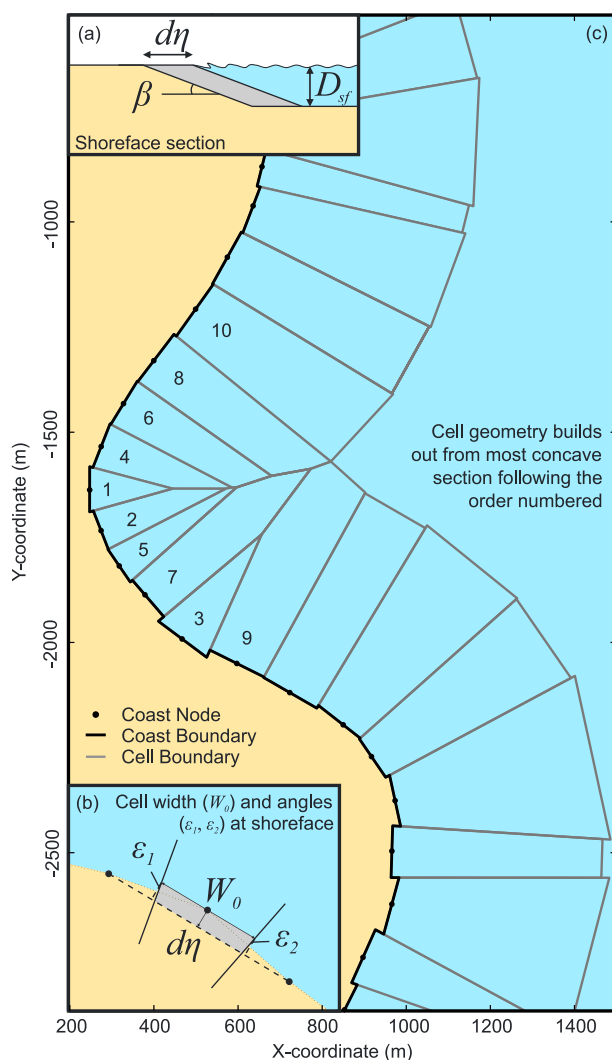
Figure 3. (a) Profile view of the shoreface showing planar equilibrium beach profile assumed to be maintained by the model. Change in shoreline position $d\eta$ results in the shoreline advancing over or retreating across a flat bottom at D_{sf}. (b) Detailed plan view of the geometry of an evolving cell. The change in shoreline position is perpendicular to the cell orientation defined by the line connecting two adjacent nodes. Cell boundaries at the upper shoreface are perpendicular to the line connecting the cell node to each adjacent node (black dots). (c) Example plot of coastal cells and their boundaries. Coastal cells are built by projecting cell boundaries seaward, starting with the most concave coastal cells. Boundaries are projected until they intersect or until D_{sf} is reached (numbered cells show the order in which the cells were built). When boundaries intersect the mean orientation of contributing cell edges determines the direction in which the projection is continued. This method results in two possible cell types, trapezoids (e.g., unnumbered cells), and polygons (e.g., cells numbered 1–10).

3.2. Shoreline Geometry

The cross-shore profile is assumed to maintain a constant time-averaged form (Figure 3a). Shoreline position evolves perpendicular to the local orientation of the shoreline ϕ [°] (Figure 3b). Use of such a local coordinate system was proposed by *LeBlond* [1972] and recently implemented in the numerical model developed by *Kaergaard and Fredsoe* [2013a] [see also *Kaergaard and Fredsoe*, 2013b, 2013c]. Similar to *Kaergaard and Fredsoe* [2013a], we represent the coastline using a vector-based approach (the coastline is represented as a series of points in Cartesian space x and y with subscripts $i = 0, 1, 2, .., n$). For each node the local orientation of the coastline ϕ is defined as the azimuthal direction of the vector connecting the two nodes adjacent to the node of interest (dashed line in Figure 3b). The cell width W_0 [L] is measured at the shoreface parallel to ϕ. For each node in the shoreline model the local shoreface has a constant slope β [°] extending down to the shoreface depth D_{sf} [L] (Figure 3a). Coastal cell boundaries are established perpendicular to lines connecting two adjacent nodes and relate to ϕ by angles ϵ_1 and ϵ_2 [°] (Figure 3b). These angles are negative when the shoreline is convergent and positive when divergent. Cells that occur at convex-out headlands widen offshore, and cells in concave embayments narrow offshore (Figure 3c). When a convex shoreline cell extends to D_{sf} the cell geometry is trapezoidal in planform. Conversely, when the coast is highly concave the cell boundaries may intersect at a depth shallower than D_{sf} resulting in triangular cells and overlapping non-adjacent cells. We developed a simple cell-building algorithm that generates the planform geometry of all cells in the coastline to accommodate variable cell geometry. A discretization scheme is implemented that divides the shoreline into a series of triangular, trapezoidal, and polygonal cells with known surface area A [L²] that allows us to conserve mass, and we develop expressions for volume change as a function of $d\eta$ in order to solve for the positional change at the coast.

The algorithm uses a priority queue ordered by the cell water depth D_c [L] to which the cell extends to process the most concave cells first (i.e., the most acute triangular cells which have the lowest D_c). For each node i in the priority queue the intersection point of the cell boundaries is found and the equivalent depth on the
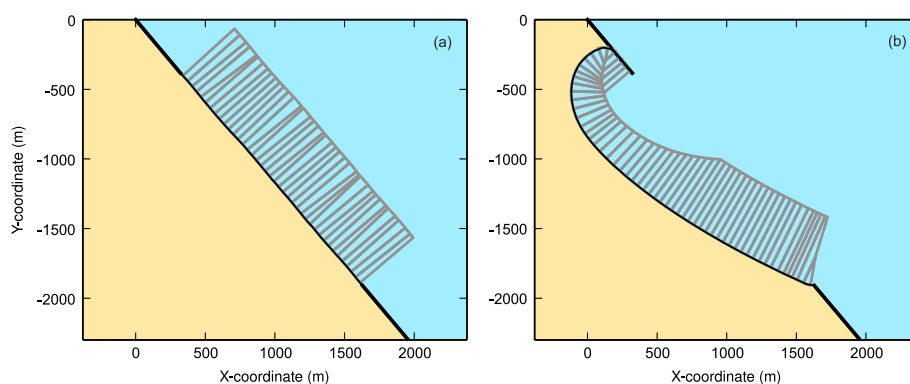
Figure 4. Coastal cell geometry for a model instance at (a) the beginning of a model run starting with a straight coastline with superimposed low amplitude noise in the coastline position and (b) the end of a model run when an equilibrium form spiral-shaped bay has formed.

shoreface D_c is calculated; the intersection becomes a vertex for the shoreline cell. The nearest unprocessed cells up and down the coastline (cells a and b) are then found and the intersection for node i also become a vertex for cells a and b. A new vector describing the cell boundary can then be described extending from the intersection point offshore at an orientation perpendicular to the mean orientation of all contributing nodes ϕ_c. The intersections between this cell boundary and the edge of nodes a and b are found and their D_c is calculated. The cell with the shallowest D_c is then added to the priority queue such that the cell-building algorithm builds outward from the most concave cell consistent with the order numbered in Figure 3c.

Alongshore sediment flux is calculated using equation (4) for each node, with breaking wave angles α_b taken relative to the local shoreline orientation between the node of interest and its adjacent downcoast neighbor (where downcoast refers to cells further along the vector, with the sea always to the left when facing down-vector, the direction in which vector index i increases). Positive angles for α_b result in positive along-shore transport directed downcoast (i.e., from cell i to cell $i+1$), while a negative α_b drives negative alongshore transport upcoast (i.e., from cell $i+1$ to cell i). For nodes where the changing shoreline orientation resulted in concomitant change in approaching wave angle from high ($\alpha_0 < -45°$; $\alpha_0 > 45°$) to low ($-45° < \alpha_0 < 45°$) or vice versa, the flux maximizing angle $\alpha_0 = \pm45°$ is used. The scheme for moving sediment necessitates track-ing neighboring cells in concave sections of coastline such that sediment bypassing may occur. For example, in Figure 3c cell 8 is bordered on its southern side by cells 6, 7, and 9. In such a scenario, alongshore sedi-ment transport from cell 8 would be distributed to all three of these cells. The relative amounts of sediment delivered to these cells are proportional to the length of their shared border. In the example in Figure 3c cell 8 would pass the vast majority of its alongshore flux to cell 6, with cell 7 and cell 9 only receiving small con-tributions. Such a scheme is required since cells that do not extend to the shoreface depth are not permitted to prograde/retrograde but rather fill up or empty in order to conserve mass (see section 3.3 below). The ten-dency for progradation or erosion should therefore be communicated to adjacent cells down the shoreface, so that they too advance or retreat in response to flux gradients.

As the coastline evolves, new nodes may be added by linear interpolation if the spacing between any node exceeds 1.5 times the specified initial node spacing. Similarly, nodes are deleted from the vector if the spacing drops below 0.66 times the specified spacing. The appropriate specified initial node spacing will depend on the application but should be relatively coarse (e.g., 50 m or greater) due to the simplifications inherent in the governing physics and to allow the cell-building algorithm to function efficiently (though it is possible to use node spacing as small as 5 m as was done for simulating smaller bays; see section 5.3). For illustration, Figure 4 shows the cell configuration at the beginning (Figure 4a) and end (Figure 4b) of a model run for a bay with headland separation $l_b = 2$ km for an offshore wave climate with mean and standard deviation wave directions of $\theta_{mean} = 025°$ and $\theta_{std} = 035°$, respectively (see section 5 below).

3.3. Changes in Shoreline Position
In order to solve for the change in shoreline position we need an expression for the volume change in tri-angular, trapezoidal, and polygonal cells that are generated by the cell-building algorithm. Since triangular and polygonal cells are not allowed to advance or retreat at their seaward extent (in order to avoid mass
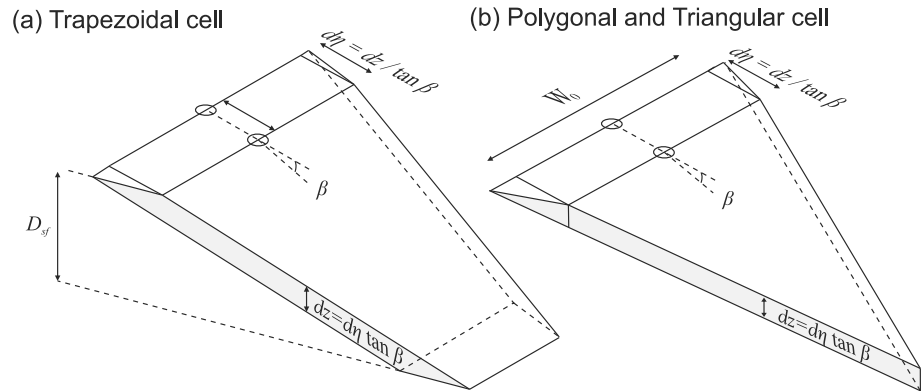
(a) Trapezoidal cell (b) Polygonal and Triangular cell

Figure 5. Geometric diagrams of the volume of change within a coastal cell for (a) trapezoidal cells, which can advance and retreat across the shoreface and (b) polygonal or triangular cells whose position at their seaward tip or boundary is fixed to prevent mass balance difficulties. The volumes of these shapes can be solved to be a function of $d\eta$. Thus, if volume change is known, we can solve for $d\eta$ following equation (5) or equation (8).

conservation errors), they have a common solution, whereas trapezoidal cells can advance or retreat across the shelf (see Figure 5). Were triangular or polygonal cells allowed to prograde, they would build out over the top of adjacent cells and sediment would be required to spill into adjacent cells. This seems to be the reason that *Kaergaard and Fredsoe* [2013a] required an iterative scheme to conserve mass in their model. Our discretization of the coast avoids this problem.

3.3.1. Low-Curvature Shorelines: Trapezoidal Cells

Figure 5a shows the volume change ∇V associated with a trapezoidal cell. Basic trigonometry allows us to formulate a quadratic solution for this volume as a function of the change in shoreline position $d\eta$:

$$\nabla V = a_1 \, d\eta^2 + b_1 \, d\eta \tag{5}$$

where coefficients a_1 [L] and b_1 [L^2] are described by the geometric properties of the cell (see Figure 3b):

$$a_1 = \frac{D_{sf}}{2}(\tan \epsilon_1 + \tan \epsilon_2) \tag{6}$$

$$b_1 = W_0 \, D_{sf} + \frac{D_{sf}^2}{2 \tan \beta}(\tan \epsilon_1 + \tan \epsilon_2) \tag{7}$$

Equation (5) is inverted for $d\eta$ using the quadratic formula with a negative solution indicating shoreline retreat and positive shoreline advance.

3.3.2. High Planform-Curvature Shorelines: Polygonal/Triangular Cells

Figure 5b shows a schematic volume of change ∇V for a triangular cell. Again we derived a solution for this volume as a function of the change in shoreline position $d\eta$ using trigonometry, resulting in a cubic expression for triangular or polygonal cells:

$$\nabla V = a_2 \, d\eta^3 + b_2 \, d\eta^2 + c_2 \, d\eta \tag{8}$$

where the coefficients a_2 [dimensionless], b_2 [L], and c_2 [L^2] are again functions of the cell geometry (see Figure 3b):

$$a_2 = -\frac{1}{6}(\tan \epsilon_1 + \tan \epsilon_2) \tan \beta \tag{9}$$

$$b_2 = \frac{1}{2}W_0 \tan \beta \tag{10}$$

$$c_2 = A \tan \beta \tag{11}$$

Equation (8) is inverted for $d\eta$ following methods presented in *Press et al.* [1992] with a negative solution indicating shoreline retreat and positive shoreline advance.
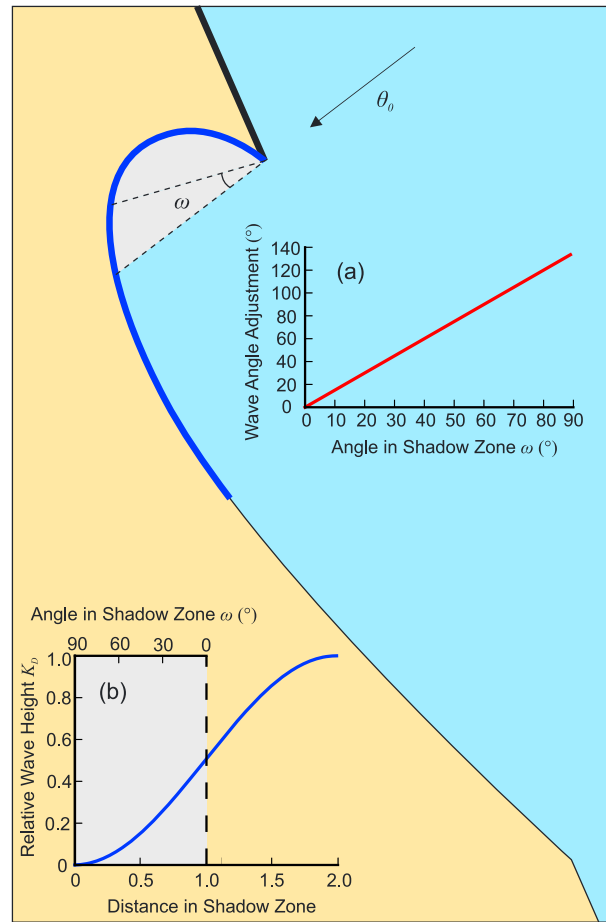
4. Wave Transformation

Expressions for alongshore sediment transport such as equation (4) require predictions of the breaking wave height and angle. We drive the model with an offshore wave distribution and transform waves to the coast using linear wave theory, similar to previous modeling approaches [e.g., *Ashton and Murray*, 2006a] (see Appendix A). These simplifications are appropriate for low planform-curvature, open coasts but additional modifications are required to account for diffraction and refraction in shadowed regions where these assumptions may not be appropriate. Therefore, in addition, we include simple rules for the diffraction and refraction of waves when the coast is shadowed from incoming waves (Figure 6).

We do not explicitly model the diffraction of waves in the shadow zone but instead rely on simple rules to modify the wave angle and wave power approaching the coast guided by the work of *Rea and Komar* [1975], *Kraus* [1984], and *Weesakul et al.* [2010]. The wave approach angle in the shadow zone θ_s [°] (Figure 6a) is prescribed following [*Kraus*, 1984; *Weesakul et al.*, 2010]:

$$\theta_s = 1.5 \left(\left| \omega - \theta_0 \right| \right) \qquad (12)$$

where ω [°] is the angle between the shadowing and shadowed cell with respect to the wave approach angle and θ_0 is the offshore wave approach angle (Figure 6). The approaching wave height within the shadow zone H_s is calculated by modifying the offshore wave height using a diffraction coefficient K_D [dimensionless] which is a function of ω [*Rea and Komar*, 1975; *Kraus*,

Figure 6. Schematic diagram of an embayment to demonstrate shadowing and wave adjustment in the shadowed region. The shadow zone is generated with respect to the offshore wave direction θ_0. The angle within the shadow zone is defined by ω. The length of coast affected by rules for diffraction is twice the length of the shadow zone as shown by the length of coast highlighted in blue. (a) Adjustment of wave approach angle by factor 1.5 times the angle within the shadow zone ω (equation (12)). The adjustment only proceeds up to $\omega = 90$ since wave heights are zero beyond this value. (b) Reduction in wave height due to wave crest spreading, which is defined by a sinusoidal function (equation (13)) with the wave height at the edge of the shadow zone assumed to be reduced by a factor of 0.5 with that factor increasing to 1 at $\omega = 90$. Wave heights outside the shadow zone are also reduced to conserve wave energy following equation (14).

1984] (Figure 6b). When a wave travels past a structure or headland it will be truncated, and the wave crest will spread into the shadow zone behind the obstruction. Simplifying from *Kraus* [1984], we approximate the resulting diffraction by assuming that along the edge line of the shadow zone, the wave height is reduced by a factor of 2 (i.e., $K_D = 0.5$). This implies that half of the wave energy has been lost due to wave crest spreading into the shadow zone. The diffraction coefficient is then modified as a function of the angle in the shadow zone (Figure 6b):

$$K_D = 0.5 \cos \omega \qquad (13)$$

In order that wave energy is conserved, the length of the coast in the shadow zone l_s [L] is determined and wave energy is also reduced downdrift of the shadow zone over the same distance. While the distance back

to the shadow zone $x_s < l_s$, where $x_s = 0$ at the tip of the shadow zone (i.e., where $\omega = 0°$; see Figure 6b), wave energy outside the shadowed zone is reduced following:

$$K_D = \frac{1}{2}\left(1 - \sin\left[90\frac{x_s}{l_s}\right]\right);$$

(14)

The diffracted wave properties were subsequently further refracted during shoaling in the same manner as waves approaching the open coast in order to predict breaking wave height and angle which drive alongshore transport (see Appendix A for description of wave transformation procedure).

5. Model Setup

5.1. Initial and Boundary Conditions
Initial model coastlines were straight and 2 km in length with an initial node spacing of 50 m. Modeled shorelines were insensitive to this initial node spacing providing it was not too coarse (more than 20 nodes were required; maximum of 100 m node spacing). The bounding ends of the coastline were fixed to represent headlands or fixed structures such as sea walls. Should the coastline erode in behind these fixed boundaries, it also becomes fixed to the landward side of the boundaries. No sediment transport was permitted into the model domain across these boundaries, but sediment was permitted to escape out of the model domain by alongshore transport. The offshore boundary is the bottom of the shoreface D_{sf} as shown in Figure 3a. For all simulations the shoreface depth was fixed to $D_{sf} = 10$ m and the shoreface slope was fixed to $\beta = 0.02$. The model time step is adaptive such that if no solution to equation (5) or equation (8) is found (e.g., due to passing too much sediment and overfilling a cell), the prescribed time step (0.1 days here) is halved iteratively until a solution is achieved, and this reduced time step persists (using the same wave conditions) until it has satisfied the length of the prescribed time step, whereupon the model returns to the prescribed time step.

5.2. Wave Climates
We test two different approaches to representing an idealized wave climate. In the first, offshore wave directions θ_0 [°] are drawn from Gaussian functions defined by mean θ_{mean} and standard deviation θ_{std}. Offshore wave height H_0 [L] and period T [T] were also described using a narrow Gaussian function with $H_{mean} = 1$ m and standard deviation $H_{std} = 0.1$ m, and $T_{mean} = 6$ s and $T_{std} = 1$ s. Second, we follow the approach of *Ashton and Murray* [2006b] using a wave climate defined by two parameters: A_s, the asymmetry (the fraction of waves approaching from left relative to the orientation of the whole coastline), and U_h, the proportion of waves which are high angle (i.e., $> 45°$ relative to the general trend of the coastline). In this case $H_0 = 1$ m, and $T = 6$ s. Wave heights, angles, and periods were then drawn from these distributions using a random number generator at each model time step.

5.3. Model Ensembles
We ran COVE using ensembles of each type of wave climate, in which the controlling parameters (θ_{mean} and θ_{std}, U_h, and A_s, respectively) were varied systematically in order to explore wave climate control on bay morphology. The range of parameter values are shown in Figures 8 and 14. The experiments were run on bays with $l_b = 2$ km and we simulated 100 years in order that all model runs attain a morphological steady state, defined by the condition that the coastal length tends to a constant value and mean change in coastline position $\overline{d\eta}$ fluctuates about zero. We ran these ensembles for the condition where wave properties in the shadow zone were diffracted following equations (13) and (14), or where there was no diffraction so that shadowed regions of the coast were not subject to sediment transport for a particular wave approach angle (similar to *Littlewood et al.* [2007]). Additionally, we ran an ensemble of experiments in which the wave climate was held constant ($\theta_{mean} = 025°$ and $\theta_{std} = 30°$, respectively), and l_b was varied over 2 orders of magnitude to explore the influence of spatial scale on bay evolution and morphology. In these experiments, the node spacing was reduced where necessary to ensure a minimum of 20 nodes representing the coastline. Model results are insensitive to node spacing smaller than this threshold.

6. Results

Model simulations evolved the coastline toward a steady equilibrium form, driven by obliquely incident waves, as demonstrated in Figure 7. Evacuation of sediment from the bay proceeds from the upcoast end
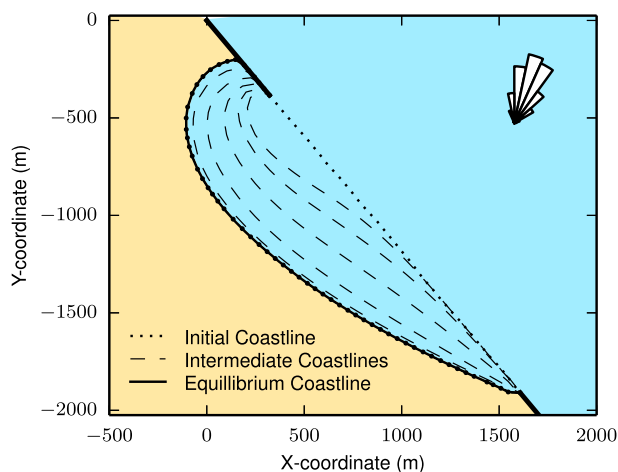
Figure 7. Evolution of bay morphology toward an equilibrium morphology between two fixed headlands/sea walls (thick black lines). Wave conditions are $\theta_{mean} = 20°$ and $\theta_{std} = 25°$, as shown by the wave rose. Model evolution starts from a straight coastline and the boundary conditions allow sediment to exit the model domain at either boundary by alongshore transport but sediment is not permitted to enter the bay from outside the domain.

since there is no sediment provided at this model boundary and alongshore transport carries sediment downcoast (similar to initial "rotation" observed by *Daly et al.* [2015]). Rules for diffraction allowed wave energy into the shadow zone behind the northern seawall/headland allowing the coastline to cut back behind this structure. Once the spiral shape has developed the shoreline is translated landward, perpendicular to the local orientation.

6.1. Modeled Equilibrium Bay Morphology

Ensemble modeling of a range of simulated wave conditions, represented by varying θ_{mean} and θ_{std} for conditions where simple rules for refraction and diffraction in the shadow zone have been included (equations (13) and (14)) are shown in Figure 8. Bay morphology is sensitive to both the dominant wave direction θ_0 and the spread of wave directions θ_{std}. Note that the bottom left portion of the plot, colored gray, is labeled for high-angle wave instability (HAWI) since this phenomenon leads to the formation of flying spits in this part of the wave climate domain, which extend from the leading end of the modeled coast, thus these results have not been included in subsequent analyses. Figure 9a shows the equilibrium coastal morphology for a transect through the wave climate space for $\theta_{mean} = -30°$. The planform relief of the bay cut into the updrift section of the coast increases with reduced wave climate variability. With low wave climate variability the majority of wave directions during the evolution to equilibrium act to transport sediment toward the southeast and out of the model domain. With increasing wave climate variability there are more waves that reverse the alongshore sediment transport direction, toward the northwest, therefore pushing sediment back into the embayment,
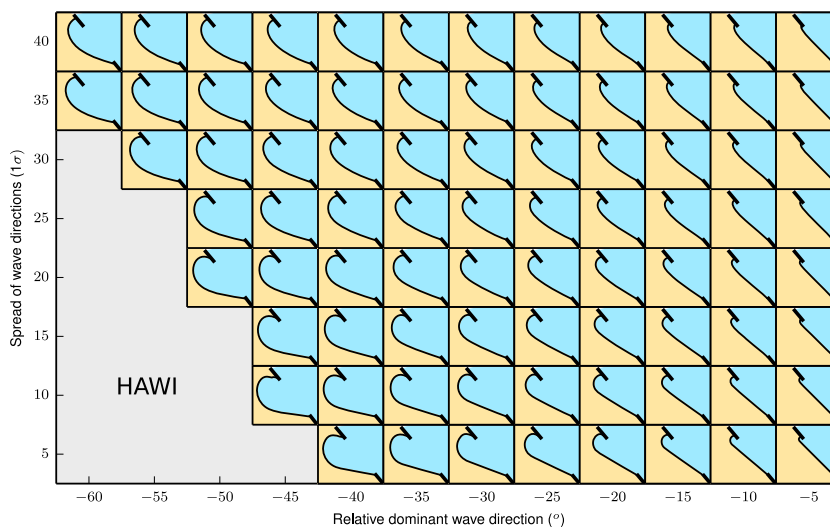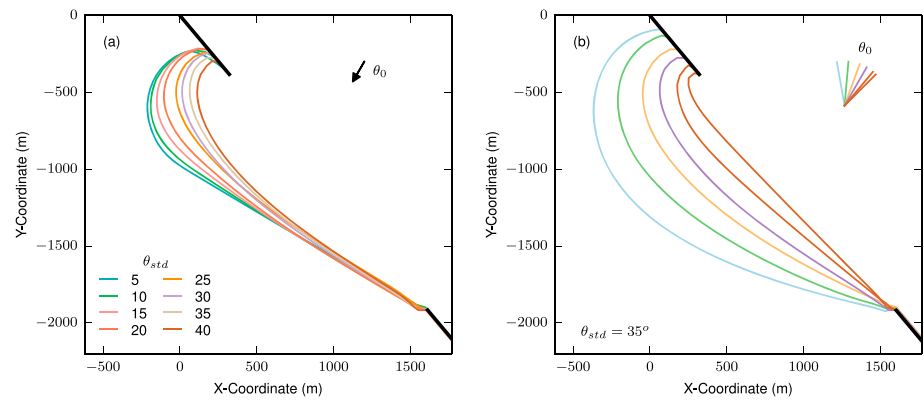

Figure 8. Final bay morphologies as a function of wave climate for normally distributed offshore wave directions described by a dominant wave direction θ_{mean} and standard deviation wave direction θ_{std}. Wave approach angles are relative to the overall orientation of the coastline (i.e., the line connecting the two headlands). For high-angle wave directions and low wave spreading high-angle wave instability (HAWI) prevents a bay from forming between the two headlands, resulting in a spit forming of the tip of the southeastern boundary.

Figure 9. Variation in bay morphology as a function of (a) spread of wave angles ($\theta_{mean} = 30°$) and (b) variation of the dominant wave direction θ_{mean} ($\theta_{std} = 35°$). Increasing the spread of wave directions decreases the embayment depth at the shadowed end of the bay since with increasing wave spread there are more waves acting to reverse alongshore transport and move sediment back into the bay. Increasing the obliquity of wave approach angles results in deeper bays for similar reasons, since less waves act to reverse alongshore transport and move sediment back into the bay.

altering the local shoreline orientation until net alongshore sediment flux is zero. Figure 9b shows the equilibrium coastal morphology for a transect through the wave climate space for $\theta_{std} = 30$. These result holds across all values of θ_{mean} and θ_{std} as shown by plots of the aspect ratio (distance between headlands divided by planform bay relief) of the modeled bays (Figure 10).

The shoreline in the unshadowed portions of the modeled embayments (southeast end of the model domain) tends toward an orientation perpendicular to θ_0 such that the coast is "swash aligned," and the net alongshore sediment flux approaches zero. For wave climates with a narrow spread of directions this section of coastline tends to be very straight, since the extent of the shadow zone updrift varies little. However, for wave climates with higher θ_{std} the downdrift end of the bay tends to be curved, as the shadowing effect reduces wave heights outside of the shadow zone due to wave crest spreading (Figure 9a). We illustrate this further by plotting histograms of shoreline curvature (calculated as the inverse of the radius of a circle passing through three adjacent nodes) as a function of θ_{std} (Figure 11). For low θ_{std} the histograms are strongly bimodal with the coastline well described by a highly curved section and straight section, but as θ_{std} increases the strength of this bimodality decreases and curvatures become more distributed.

6.2. Evolution to Equilibrium

For a 2000 m headland separation, the coastlines shown in Figure 8 approached an equilibrium form in < 40 years in all cases. Figure 12 summarizes the evolution of several model runs with $l_b = 2000$ m and $\theta_{mean} = 025°$
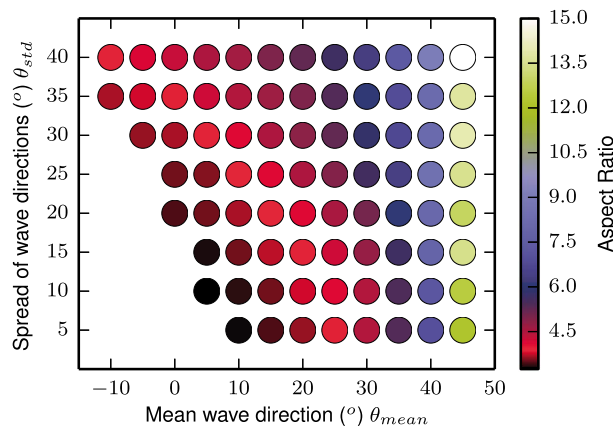

Figure 10. Variation in the aspect ratio of equilibrium bays as a function of wave climate. Aspect ratio increases under more shore-normal wave approach angles and with a greater spread in wave directions as the depth of the bay decreases.

toward equilibrium by showing the change in length of the bay through time (Figure 12a). The coastline was characterized as having attained equilibrium once its length had attained 99% of the mean value over the last 10 years of simulation. Figure 12b shows the time to equilibrium T as a function of the variability in wave climate. The kinked nature of this plot likely reflects competition between two main factors: increased variability delivering more wave energy to shadowed regions encouraging more rapid evolution θ_{std}=15–30; more frequent occurrence of waves that act to push sediment back into the bay when θ_{std}=30–40°. Figure 12c shows the mean change in coastline position
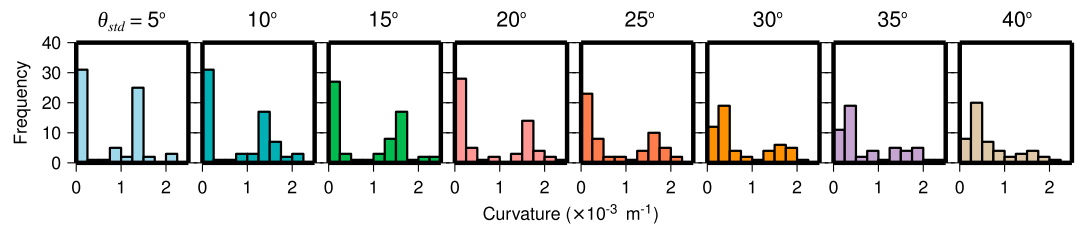
Figure 11. Histograms of shoreline planform-curvature as a function of the variability of the wave climate θ_{std} for $\theta_{mean} = 015°$. Where the variation in the wave climate is low, the bays have a strongly bimodal distribution of curvature, with a high-curvature hooked zone and a low-curvature straight section. With increasing wave angle variability this bimodality becomes more spread and these zones merge.

through time, which fluctuates about zero once equilibrium has been attained. For more variable wave climates (large θ_{std}) the mean change in coastal position through time can be more variable, as reversals in the direction of alongshore sediment transport occur more frequently (Figure 12d), with waves directed from the southeast able to push sediment back into the bay. If these changes were more persistent (e.g., due to seasonal variations) such conditions would be expected to lead to bay rotation [e.g., *Harley et al.*, 2011; *Turki et al.*, 2013; *Ratliff and Murray*, 2014].

Figure 13 illustrates the evolution of embayed beaches toward equilibrium for different lengths of bay l_b. We nondimensionalize the horizontal coordinate system by dividing through by l_b to give nondimensional coordinates $X*$ and $Y*$ and allow comparison of bay morphology for different spatial scales subject to the same wave climate. Figure 13a shows dimensionless equilibrium bay morphology forced by a wave climate characterized by $\theta_{mean} = 025°$ $\theta_{std} = 20°$. There is no systematic variation in planform morphology with l_b and thus the predicted morphologies in Figure 8 are expected to scale with l_b. We stress that the simplified representation of physical processes may be inappropriate for modeling where $l_b < 1$ km but include these scales for comparison to the results of [*Daly et al.*, 2014]. Figure 13b shows the evolution of bay length for these simulations in logarithmic space. Bay length eventually asymptotes as an equilibrium morphology emerges. The timescale T taken to attain equilibrium during these simulations is plotted against l_b in Figure 13c. We find that this timescale scales with the square of the distance between the headlands, such that a 1 km bay would take ~10 years to reach equilibrium yet a 16 km bay takes ~2560 years. This implies that the size of a
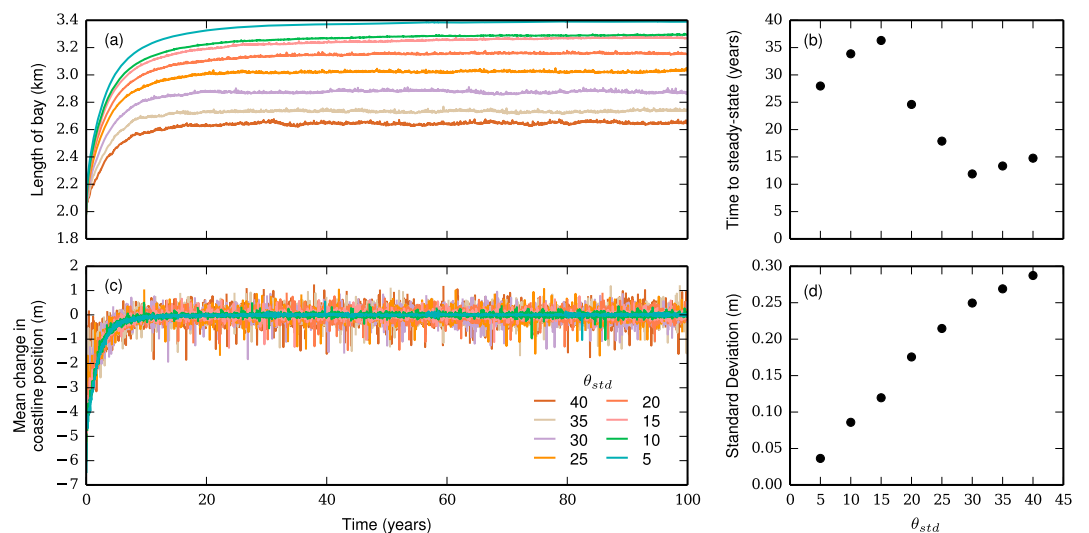

Figure 12. (a) The evolution of bay length through time for $\theta_{mean} = 25$ as a result of changing θ_{std}. (b) Time required to attain morphological steady state for model runs shown in Figure 12a), where steady state is defined as the time required to attain 99% of the final coastline length, which is <40 years in all cases. (c) Mean change in coastline position through time for the simulations shown in Figure 12a. (d) Standard deviation of mean coastline position change between 60 and 100 years (after attainment of steady state) showing that fluctuations along the coastline are driven by the variability of the wave climate (θ_{std}).
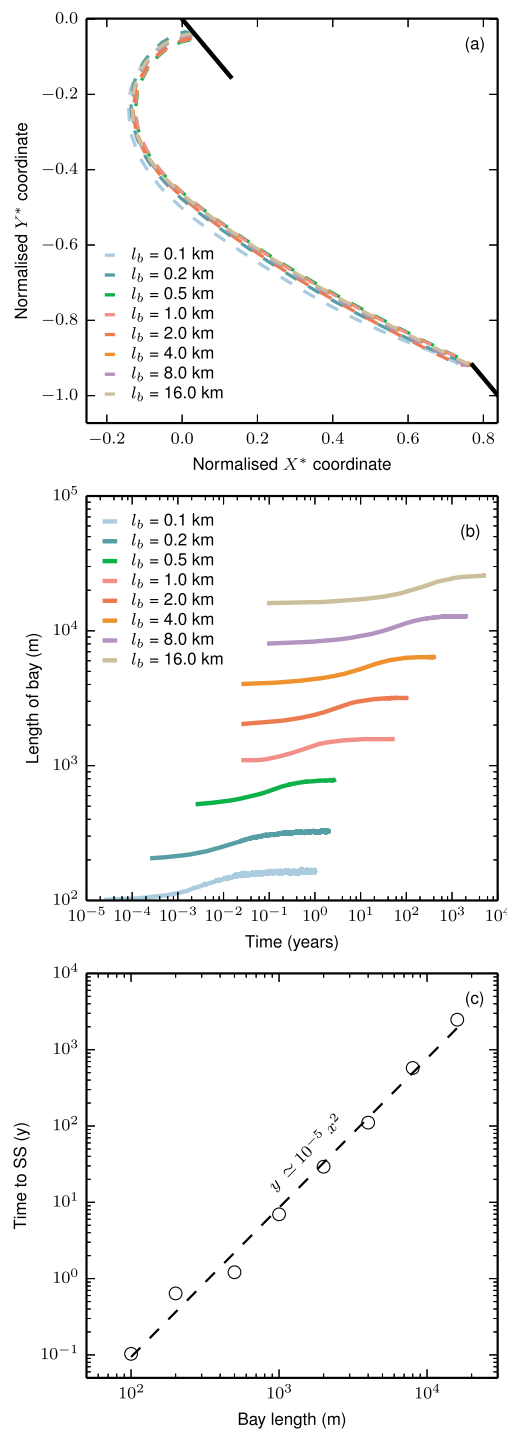
Figure 13. (a) Nondimensional equilibrium form of modeled bays varying the length between the headlands subjected to identical wave climates ($\theta_{mean} = 025°$, $\theta_{std} = 20°$). Nondimensional coordinates were calculated by dividing coordinates by the length between the headlands ($X*= X/l_b$, $Y*= Y/l_b$). (b) Coastline length through time for different bay sizes showing that length tends toward a constant value when equilibrium has been attained. (c) Time to equilibrium as a function of bay size. Dashed line represents a linear regression of log-transformed values showing that the time to equilibrium scales with the square of bay size.

bay is important in determining its response to and recovery from perturbations such as storms or prolonged changes in wave climate.

6.3. Characterization of Wave Climate

Figure 14 shows the morphological predictions using wave climates parameterized following *Ashton and Murray* [2006a] (see section 5.2). For the highest combination of $A_s > 0.85$ and $U_h > 0.8$, high-angle wave instability led to the formation of flying spits hanging from the model domain, so these results are not included. The formation of crenulate-shaped bays is favored by a strongly asymmetric wave climate, so that there are fewer waves that reverse the dominant direction of alongshore transport. Increasing the fraction of high-angle waves U_h tends to lead to higher-relief bays which are more symmetric in planform. Simulations with high asymmetry and a low fraction of high-angle waves resulted in crenulate-shaped bays. Due to the high spread of wave angles inherent to this characterization of wave climate, bay morphologies are similar to those characterized by high θ_{std} in Figure 8.

6.4. Influence of Wave Diffraction on Bay Morphology

Modeling experiments were carried out both with and without rules for diffraction in the shadow zone. In the absence of diffraction, no sediment transport occurs at all in the shadow zone. Figure 15 compares equilibrium coastlines when diffraction is included (solid line) and ignored (dashed line) for various values of θ_{std} and $\theta_{mean} = 20°$. Comparing the dashed and solid lines, we can see that some unrealistic embayment shapes emerge when diffraction is neglected. This is true for narrow ranges in wave angle, which may result in acute angles in the coastline, since only a small proportion of waves are able to influence the region that is usually shadowed, and these waves tend to be highly oblique to the shadowed coast. Such restricted, high-angle wave climates are unlikely in nature. For broader ranges in wave angles (high θ_{std}) diffraction appears less important and modeled coastlines with and without diffraction are similar; the main difference being the straightness of the coast outside the shadowed region. Diffraction reduces wave heights outside of the shadow zone due to wave crest spreading. The results concur with the recent study by *Daly et al.* [2014], who demonstrated that wave diffraction is a dominant control on bay morphology only for wave climates with restricted approach angles.
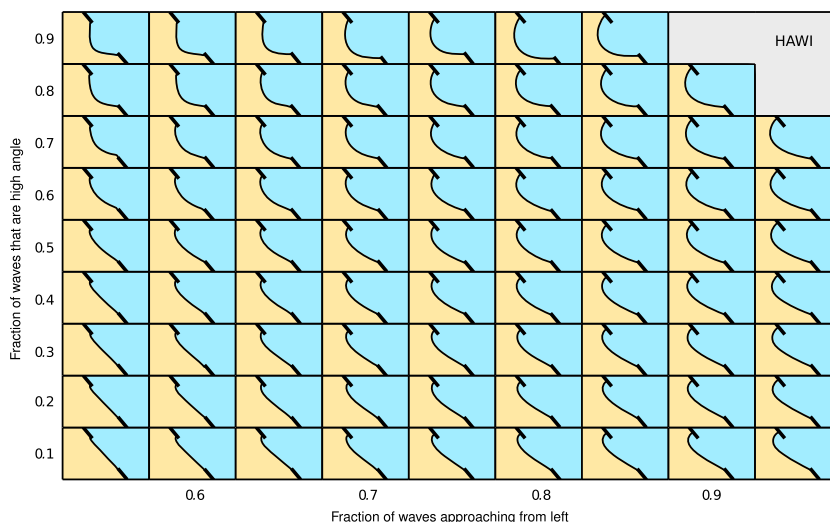
Figure 14. Bay morphologies predicted by wave climates defined by asymmetry and highness (proportion of waves that are high angle). Crenulate-shaped bays develop with high wave climate asymmetry and for all but the highest fraction of high-angle waves. A high fraction of high angle waves tends to produce more symmetric bay shapes. Note again that high angle wave instability (HAWI) prevented some model runs from achieving as stable bay morphology due to the formation of spits at the downdrift boundary.

7. Discussion

Our results above show that the planform morphology of embayments is sensitive to both the dominant wave direction and the spread of wave directions impinging on the coast. For a given dominant wave direction, the morphology of the bay can vary depending on the spread of wave directions (θ_{std}), tending toward a morphological steady state in which there is little variation in shoreline position through time, and zero net alongshore sediment flux. We demonstrate that the time for a bay to evolve to its equilibrium condition scales with the square of the distance between the two headlands. This diffusion-like scaling suggests that small bays may respond to and recover from perturbations in wave conditions rapidly, while larger bays may take substantially longer. Using the Delft3D model, *Daly et al.* [2015] performed comparative simulations with bay lengths of 140, 300, and 600 m, and estimated response times of 2, 15, and 1200 years, respectively. This generally supports our finding that there is nonlinear dependence 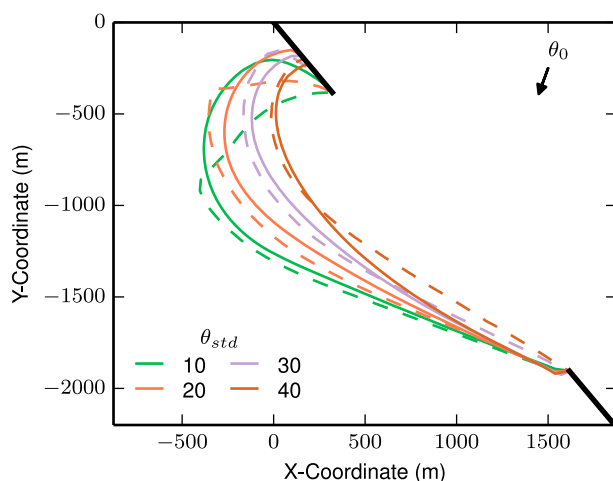of response time to bay size. For similar bay lengths simulated in this study and plotted in Figure 13c, we predict response times of approximately 0.2, 0.8, and 3.5 years, respectively, significantly shorter than those of *Daly et al.* [2015]. These differences likely relate to the parameterization of sediment transport formula, which carry significant uncertainties. Calibrations of the transport coefficient K_{ls} in equation (4) have shown it to be quite variable on sandy beaches but may correlate to grain size, beach slope, or wave characteristics [*Van Wellen et al.*, 2000]. Indeed, the simulations by *Daly et al.* [2015] demonstrate a strong dependence of response time on grain size. The use of alternative transport formulae has been demonstrated to produce broadly similar results to the CERC equation used in this study [*Ashton and Murray*, 2006b]. The choice of alongshore sediment transport

Figure 15. Comparison of bay morphology between model runs with rules for diffraction included (solid lines) or omitted (dashed lines). θ_{mean} was 20°. Bay morphologies are similar for high values of θ_{std} but not for low θ_{std} where unrealistic sharp angles in the coastline develop when diffraction is not included.
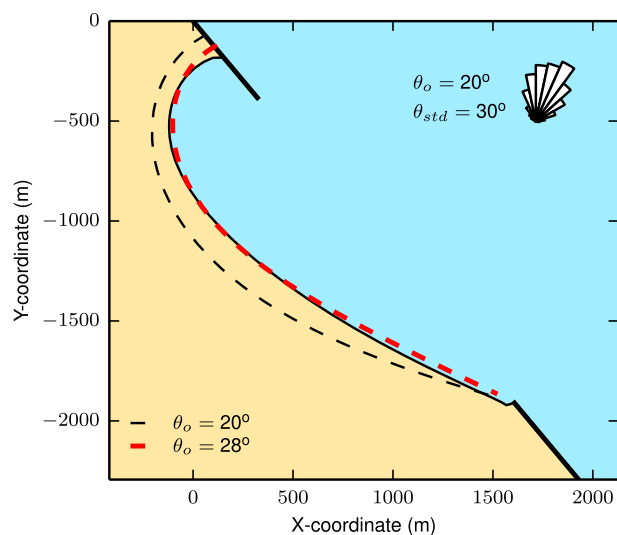
Figure 16. Predicted steady state bay morphology for $\theta_{mean} = 20°$ and $\theta_{std} = 30°$. Dashed lines show the prediction of the parabolic bay equation [*Hsu and Evans*, 1989] using the dominant wave approach angle taken from the model parameters $\theta_{mean} = 20°$ (black) and the best fit parabolic bay treating dominant wave approach angle as a free parameter (red; best fit $\theta_0 = 28°$).

formula (e.g., equation (4)), its calibration parameters, as well as other factors in the model such as the choice of shoreface depth D_{sf}, slope β and variations in wave height H_0 will influence the time taken to reach equilibrium but we would not expect them to change the quadratic dependence of time to equilibrium on bay size. Sediment fluxes depend on shoreline orientation, and the planform configuration of the bays are consistent between scales, in a self-similar sense. What changes is the alongshore distance over which erosion (or progradation) occurs and the cross-shore distance over which shoreline position needs to change to produce the same proportional change in bay morphology. Both of those factors scale with l_b, therefore the amount of sediment transport needed to approach equilibrium (by any given amount) scales as l_{b^2}, while the fluxes do not vary with l_b. This leads to T proportional to l_{b^2} robustly. Our model results are consistent with this.

The shoreline may still fluctuate about an average state in response to fluctuations in the wave climate and reversals in alongshore sediment transport direction, with sediment shifted from one end of the model domain to the other causing beach rotation [e.g., *Harley et al.*, 2011; *Turki et al.*, 2013]. Additionally, *Ratliff and Murray* [2014] identified "breathing" in time series of embayment shoreline positions due to sediment exchanges between the central part of the bay and the edges. They interpreted this mode as the result of stochastic variation in the occurrence of high-angle waves for a particular wave climate, modifying its diffusivity. Variations in beach planform morphology have previously been attributed to changes in external forcing (e.g., shifting wave climates at seasonal to decadal timescales [e.g., *Harley et al.*, 2011; *Thomas et al.*, 2011]), yet interestingly, *Ratliff and Murray* [2014] identified that similar timescales for morphological fluctuation emerge from internal dynamics of coastline models forced by a constant wave climate. Similar to our study, *Ratliff and Murray* [2014] explore beach rotation in response to alongshore sediment transport, but shoreline rotation can also be caused by alongshore gradients in cross-shore sediment transport [*Harley et al.*, 2011]. Indeed cross-shore sediment dynamics may play an important role in the evolution of nearshore bathymetry, which in turn influences the delivery of wave energy to the shoreface. The relative influence of these two transport modes in controlling shoreline rotation could be further explored by coupling cross-shore and alongshore sediment transport [e.g., *van den Berg et al.*, 2012]. We do not explore seasonal changes in wave forcing in this study and as such fluctuations about the average equilibrium state are relatively small. Future work could consider rotation and recovery of embayments in response to storms and storm sequences, and seasonal changes in wave climate.

Empirical formulae for bay morphology are cast as a function of the dominant wave angle only and therefore are unable to account for wave climate variability. Here we compare the model predictions to these empirical formulae to try to understand how their parameters may be controlled by the nature of the wave climate. We go on to discuss model limitations and future work.

7.1. Empirical Formulations for Embayment Morphology
7.1.1. Parabolic Bay Equation
The parabolic bay equation (equation (2)) predicts the static equilibrium bay morphology in reference to a specified diffraction point. Figure 16 shows the predicted bay morphology generated by the numerical model for a Gaussian distributed wave climate with $\theta_{mean} = 20°$ and $\theta_{std} = 30°$, and the corresponding empirical

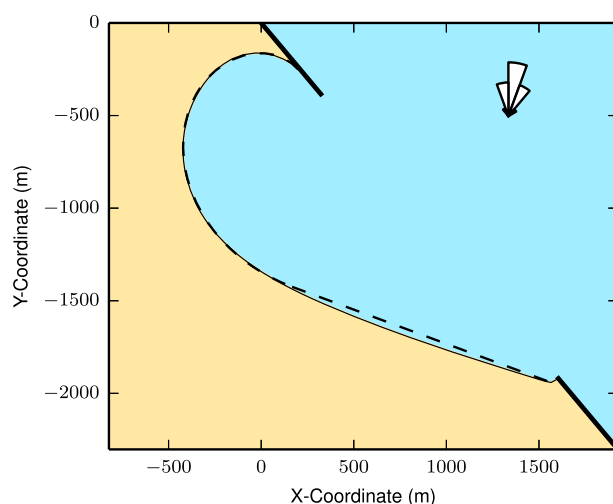**Figure 17.** Predicted steady state bay morphology for $\theta_{mean} = 10°$ and $\theta_{std} = 20°$. Dashed line shows the best fit logarithmic spiral, fitted to the curved part of the coastline only. A straight line is used outside of the shadowed region. Logarithmic spirals are extremely versatile and able to provide a reasonable fit to all bay shapes for model simulations where diffraction rules are included.

predictions based on equation (2). The black dashed line shows the parabolic bay prediction for the dominant wave direction $\theta_0 = 20°$, which predicts a deeper set bay than generated by the numerical model. We find that if we allow the dominant wave direction θ_0 to be a free parameter, we can find a best fit parabolic bay (using residual sum of squares regression) with an apparent dominant wave direction of $\theta_0 = 28°$ (note that the position of the downcoast control point is also a free parameter). The discrepancy is likely the result of the diffraction rules, which reduce wave heights downcoast of the shadow zone due to wave crest spreading, while wave heights for waves approaching from the east to southeast cause reversal in alongshore sediment transport. Hence, the approaching wave direction that results in zero net alongshore flux will not be normal to the local shoreline orientation. Discrepancies between numerical model results and parabolic bay predictions due to wave climate variability have also been noted by *Daly et al.* [2014].

7.1.2. Logarithmic Spiral Bay Equation

We fit logarithmic spirals (equation (1)) to the modeled coastlines for model runs in which rules for diffraction were included and wave directions had a Gaussian distribution. Equation (1) was fitted using least absolute deviation to the curved portion of the bay, defined using a threshold gradient in the orientation of the coast. The logarithmic spiral is much more versatile than the parabolic bay. It is possible to generate good fits of the logarithmic spiral to most modeled bays (e.g., Figure 17). However, this flexibility limits the use of logarithmic spirals as a predictor of embayed coastal morphologies, because there is no satisfactory relationship between wave climate and logarithmic spiral parameters. Furthermore, *Hsu et al.* [2010] note that a difficulty with the logarithmic spiral model is that the origin does not coincide with a diffraction point (i.e., the tip of the headland) and *Oliveira and Barreiro* [2010] found that origins of the logarithmic spiral fitted to beaches on the coast of Portugal did not coincide with the diffraction point. We find that from our simulations the origin of the best fit logarithmic spiral varies depending on the wave climate (Figure 18a). Defining the position of the origin (black dots) relative to the diffraction point (white circle; Figure 18a) as a vector characterized by distance and azimuth, it can be seen that the position of the origin varies systematically with the wave climate. In Figure 18b the distance to the origin (vertical axis) as a function of wave climate parameters was fitted with a six-term quadratic equation by least squares regression ($R^2 = 0.72$), this is the plotted surface (points are the raw data). The color shading shows the azimuth angle from the diffraction point to the origin. As θ_{mean} increases, the distance between the diffraction point and the headland or sea wall increases and the origin tends to move seaward. As θ_{std} decreases, the origin tends to move landward and the distance to the diffraction point increases. Additionally, the other parameters of the log spiral also vary with wave climate (Figures 18c and 18d).

7.2. Model Limitations

The model setup used in the experiments presented here assume that the headlands/sea walls are entirely fixed in order to evolve adjacent bays to a state of equilibrium. Therefore, the planform relief (distance that headlands protrude out to sea relative to beaches [e.g., *Limber et al.*, 2014]) is limited by the ability of the wave climate to evacuate sediment around the headlands. The planform morphology may be expected to differ when the headlands and bay are eroding back, such that headland-bay planform relief will be controlled by both the relative resistivities of coastal material to erosion, and the nature of the wave climate driving alongshore sediment transport [*Limber et al.*, 2014; *Limber and Murray*, 2014]. The results presented here
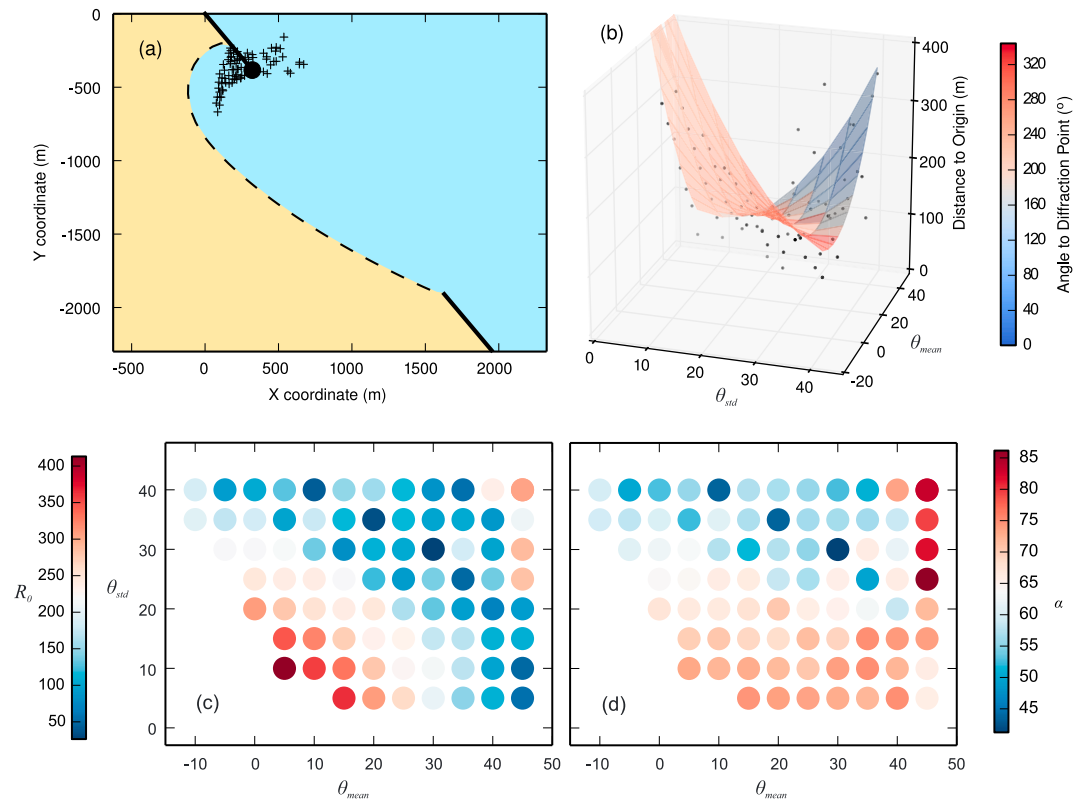
Figure 18. Variation in parameters of the log spiral as a function of wave climate. (a) Location of the origin for the best fit log spiral for all simulations plotted in Figure 8. Each is parameterized by its distance and azimuth from the diffraction point (black circle). (b) Variation in the position of the log spiral origin as a function of wave climate. Surface is a best fit six-term quadratic through the data points shown ($R^2 = 0.72$) showing the variation in the distance to the origin as a function of θ_{std} and θ_{mean}. The surface is shaded according to the azimuth from the diffraction point to the origin. The origin tends to move seaward, from the diffraction point for a combination of low-angle $\theta_{mean} = 20–40°$ and high θ_{std}, and moves landward for high angle approaching waves $\theta_{mean} = -20–0°$ and low θ_{std}. (c) Variation in the initial radius R_0 of the logarithmic spiral as a function of wave climate. R_0 generally decreases with increasing θ_{mean} and θ_{std}, reflecting that the model predicts deeper bays with decreasing θ_{std} and θ_{mean} (see also Figure 9). (d) Variation in the angle parameter α with wave climate. α shows limited sensitivity to varying θ_{mean} but tends to increase with decreasing θ_{std}.

assume there is no provision of sediment from the model boundaries, and we expect the equilibrium planform morphology of a bay will change when there is sediment flux into the bay around the headlands. The planform morphology will adjust to an equilibrium form in which it conveys sediment inputs through the bay such that time-averaged alongshore transport is approximately equal everywhere to the rate of sediment input.

We have made simple representations of wave climates, using either Gaussian distributions or a four part probability density function to represent a variety of offshore wave conditions. Wave transformation assumes linear wave theory and shore-parallel bathymetric contours, and in highly concave planform shorelines the use of simple rules for wave transformation in the shadow zone. These results are intended to explore the potential influence of variable wave climates on the morphology of crenulate-shaped bays in order to highlight that some understanding of the temporal variation of wave conditions will be important in governing the morphology of crenulate-shaped bays. Efforts to predict the morphology for specific sites would be well advised to consider collecting field data for real wave conditions and modeling wave transformation to the nearshore using a hydrodynamic model such as SWAN [*Booij et al.*, 1999] (which could be coupled to machine learning techniques [e.g., *Limber et al.*, 2014]). These could serve as input to a one-line coastal model for coastal intervention planning. These results highlight the advantages of carrying out exploratory one-line modeling to test the stability of an engineering design that was based on an empirical equation such as the parabolic bay equation [*Hsu and Evans*, 1989; *Hsu et al.*, 2010].

8. Conclusions

We present a new vector-based one-line model for the evolution of sandy coastlines which uses a local coordinate approach in order to evolve the coast relative to its local morphology and orientation. The model solves for the change in coastline position as a function of gradients in alongshore sediment transport, and uses irregularly shaped coastal cells (triangles, polygons, and trapezoids) which facilitate mass conservation. We apply the model to simulate the evolution of embayments between two fixed headlands/sea walls and find that the model is capable of successfully producing realistic bay shapes across a range of offshore wave conditions, which tend toward a condition of equilibrium. Dominant wave direction and the spread of wave directions dictate the morphology of equilibrium bay shapes, with more oblique wave directions and narrow wave direction spread encouraging bays that are cut deeper into the coast. The time taken for bays to attain equilibrium morphology is found to scale with the square of the distance between the headlands. Our results show that in the limit of narrow distributions of wave direction, including diffraction rules in a numerical model is required to produce realistic crenulate bay shapes (consistent with the findings of *Daly et al.* [2014]). Outwith this limit, diffraction still influences the morphology of the bay, resulting in bays that are more curved along their length, yet in contrast to previous studies [*Rea and Komar*, 1975; *Weesakul et al.*, 2010], diffraction is not essential to understand the formation of crenulate bays (consistent with the findings of *Littlewood et al.* [2007]). Comparison to empirical formulations for static bay morphology reveal differences in predicted bay planform morphology driven primarily by the spread of wave approach angles, suggesting that engineering solutions based on the static bay concept should consider the variability of waves impinging on the coast within a modeling framework when designing coastal interventions.

Appendix A: Wave Transformation

A1. Airy Wave Theory

Similar to previous one-line modeling studies [e.g., *Hanson*, 1989; *Ashton and Murray*, 2006a; *van den Berg et al.*, 2012; *Kaergaard and Fredsoe*, 2013a] waves are transformed following Airy/linear wave theory. The energy density of a single gravity wave is the summation of potential and kinetic components, expressed as [e.g., *Sunamura*, 1992; *Komar*, 1998]:

$$E = \frac{1}{8}\rho_w g H^2 \qquad (A1)$$

where E [M T^{-2}] is wave energy density (this is N m^{-2}), ρ_w [M L^{-3}] is the density of water, g [L T^{-2}] is acceleration due to gravity and H [L] is wave height. Assuming zero energy loss during shoaling, increasing wave height as the wave approaches the shore is balanced by a reduction in the wave speed C [L T^{-1}], so that wave power P [M L T^{-3}] is conserved:

$$P = ECn = \frac{1}{8}\rho_w g C n H^2 \qquad (A2)$$

The coefficient n relates wave velocity to the velocity of a group of waves ($C_G = Cn$) describing the evolution of wave shape with shoaling (varying between 0.5 in deep water and 1.0 in shallow) and is defined

$$n = \frac{\frac{1}{2}(1 + 2kh)}{\sinh(2kh)} \qquad (A3)$$

where k is the wave number [L^{-1}] ($k = 2\pi/L$; where L [L] is wavelength) and h [L] is water depth. The model is provided with offshore wave conditions as inputs, wave period T [T], offshore wave height H_0 [L] and offshore wave direction θ_0 [°]. These waves are then transformed from deep to shallow water assuming shore-parallel depth contours. Following Airy wave theory [e.g., *Sunamura*, 1992; *Komar*, 1998], the deep water wave velocity C_0 [L T^{-1}] and wavelength L_0 [L] are set by wave period T:

$$C_0 = \frac{gT}{2\pi} \qquad (A4)$$

$$L_0 = \frac{g}{2\pi T^2} \qquad (A5)$$

Fenton and McKee [1990] presented an approximation for wavelength as a function of wave period and water depth for waves that have not reached breaking height:

$$L = L_0 \left(\tanh \left[\sqrt{\frac{2\pi h}{L_0}} \right]^{\frac{3}{2}} \right)^{\frac{2}{3}} \tag{A6}$$

Subsequently, wave velocity is related to the deep water velocity and the wavelength at a given water depth:

$$C = C_0 \tanh \frac{2\pi h}{L} \tag{A7}$$

A2. Wave Shoaling

Assuming no refraction or loss of energy due to bottom friction, wave power P is conserved from deep to shallow water. The associated change in wave height can be described using a shoaling coefficient K_S found by equating the power of deep water waves P_0 to that of shallow waves P:

$$K_S = \sqrt{\frac{1}{2n}} \tag{A8}$$

Shoaling results in a slight reduction in wave height as a wave enters intermediate water depths, but approaching shallow water, wave height increases.

A3. Wave Refraction

As waves approach the coast they start interacting with the seabed (once within the depth of wave base $h_{wb} \approx L/2$). Wave velocity decreases as water depth h decreases (equation (A7)). Because of wave shoaling, an obliquely approaching wave slows at the shoreward end. This refracts the wave crest progressively toward the coast. Following Snells law and assuming a straight shoreline with parallel contours, the angle of wave incidence θ can be calculated as a function of the ratio of wave velocity offshore to nearshore:

$$\sin \theta = \frac{C}{C_0} \sin \theta_0 \tag{A9}$$

As the wave refracts progressively, the crest also stretches, resulting in some loss of power [*Adams et al.*, 2002]. This effect can be expressed as a refraction coefficient K_R, that is set by the offshore incidence angle of incoming waves (α_0) and the wave incidence angle approaching the shore (α):

$$K_R = \sqrt{\frac{\cos \alpha_0}{\cos \alpha_b}} \tag{A10}$$

Therefore, wave height approaching the coast can be expressed as a function of deep water wave height and shoaling, refraction, and diffraction (equation (13) and (14)) coefficients for a given water depth:

$$H = K_S K_R K_D H_0 \tag{A11}$$

A4. Wave Breaking

Typically, the water depth for the initiation of a breaking wave h_b [L] is related to breaking wave height H_b [L] by the coefficient $\gamma = 0.8$ through the relationship:

$$H_b \approx \gamma h_b \tag{A12}$$

Therefore, by iterating from deep to shallow water and updating H the height of wave breaking can be estimated and as well as the angle made by the breaking wave with the shoreline. These parameters can then be used to calculate volumes of alongshore sediment transport.

Notation

	Dimensions of [M]ass, [L]ength and [T]ime denoted in square brackets.
α_b	Angle between breaking wave crest and the local coastline orientation [°].
β	Shoreface Slope [°].
γ	Wave breaking depth coefficient [dimensionless].
ϵ_1, ϵ_1	Angles between local cell orientation ϕ and cell boundaries [°].
η	Shoreline position relative to local shoreline orientation [L].
θ	Wave approach direction [°].
θ_0	Offshore wave direction [°].
θ_{mean}	Mean offshore wave direction [°].
θ_{std}	Standard deviation of offshore wave directions [°].
θ_S	Wave approach direction in the shadow zone [°].
λ	The constant tangential angle in a logarithmic spiral [°].
κ	Angle between incoming wave crests and parabolic bay equation reference line R_0 [°].
ρ_w	Density of sea water [M L^{-3}].
ρ_s	Density of sediment [M L^{-3}].
ϕ	Local shoreline orientation [°].
ϕ_c	Cell-building orientation [°].
ψ	The angle around a fitted log spiral [°].
ω	Radial angle within shadow zone [°].
a	Upcoast cell index.
a_1	Coefficient of quadratic solution for shoreline change.
a_2	Coefficient of cubic solution for shoreline change.
A	Surface area of a coast line cell [L^2].
A_s	Proportion of waves approaching from left relative to coastline orientation.
b	Downcoast cell index.
b_1	Coefficient of quadratic solution for shoreline change.
b_2	Coefficient of cubic solution for shoreline change.
C	Wave velocity [L T^{-1}].
C_G	Wave group velocity [L T^{-1}].
C_0	Offshore wave velocity [L T^{-1}].
C_1, C_2, C_3	Empirical coefficients for empirical parabolic bay equation [dimensionless].
D_{sf}	Depth of the shoreface [L].
D_c	Depth at seaward-most extent of an individual polygonal cell [L].
E	Wave energy density [M T^{-2}].
g	Gravitational acceleration [L T^{-2}].
H	Wave height [L].
H_0	Offshore wave height [L].
H_{mean}	Mean offshore wave height [L].
H_{std}	Standard deviation offshore wave height [L].
H_b	Breaking wave height [L].
H_S	Wave height in the shadow zone [L].
h	Water depth [L].
h_b	Water depth at wave breaking [L].
i	Indices for coastal cells.
k	Wave number [L^{-1}].
K_{ls}	Empirical transport coefficient [L$^{0.5}$ T^{-1}].
K_R	Refraction coefficient [dimensionless].
K_S	Shoaling coefficient [dimensionless].
K_D	Diffraction coefficient [dimensionless].
l_s	Length of coastline within shadow zone [L].
l_b	Length of bay between two headlands/sea walls [L].
L	Wavelength [L].
L_0	Offshore wavelength [L].

n	Wave shape coefficient [dimensionless].
P	Wave power [M L T^{-3}].
Q_{ls}	Alongshore sediment transport rate [L^{3}T^{-1}].
r	Radial distance from coastline to center of a fitted log spiral [L].
r_0	Minimum radial distance from coastline to center of a fitted log spiral [L].
R_0	Reference line to point downdrift of which the coastline is linear [L].
R	Distance from control point to position of coast as a function of angle ψ [L].
s	Local alongshore coordinate [L].
t	Time [T].
T	Wave period [T] .
T_{mean}	Mean wave period [T].
T_{std}	Standard deviation wave period [T].
U_h	Proportion of waves that are high angle.
V	Volume of sediment in a coastal cell [L^3].
W_0	Cell width perpendicular to ϕ at the shoreline [L].
x	Abscissa of a coast line node in Cartesian reference frame [L].
x_s	Distance along coastline to edge of shadow zone [L].
y	Ordinate of a coast line node in Cartesian reference frame [L].

References

Adams, P. N., R. S. Anderson, and J. Revenaugh (2002), Microseismic measurement of wave-energy delivery to a rocky coast, *Geology*, *30*(10), 895–898.

Ashton, A., A. B. Murray, and O. Arnoult (2001), Formation of coastline features by large-scale instabilities induced by high-angle waves, *Nature*, *414*(6861), 296–300, doi:10.1038/35104541.

Ashton, A. D., and A. B. Murray (2006a), High-angle wave instability and emergent shoreline shapes: 1. Modeling of sand waves, flying spits, and capes, *J. Geophys. Res.*, *111*, F04011, doi:10.1029/2005JF000422.

Ashton, A. D., and A. B. Murray (2006b), High-angle wave instability and emergent shoreline shapes: 2. Wave climate analysis and comparisons to nature, *J. Geophys. Res.*, *111*, F04012, doi:10.1029/2005JF000423.

Bailard, J. A. (1984), A simplified model for longshore sediment transport, in *Proceedings of the 19th International Conference on Coastal Engineering*, pp. 1454–1470, ASCE, New York, doi:10.9753/icce.v19.%p.

Barkwith, A., C. W. Thomas, P. W. Limber, M. A. Ellis, and A. B. Murray (2014a), Coastal vulnerability of a pinned, soft-cliff coastline—Part I: Assessing the natural sensitivity to wave climate, *Earth Surf. Dyn.*, *2*(1), 295–308, doi:10.5194/esurf-2-295-2014.

Barkwith, A., M. D. Hurst, C. W. Thomas, M. A. Ellis, P. L. Limber, and A. B. Murray (2014b), Coastal vulnerability of a pinned, soft-cliff coastline. II: Assessing the influence of sea walls on future morphology, *Earth Surf. Dyn.*, *2*(1), 233–242, doi:10.5194/esurf-2-233-2014.

Bayram, A., M. Larson, and H. Hanson (2007), A new formula for the total longshore sediment transport rate, *Coastal Eng.*, *54*(9), 700–710.

Booij, N., R. C. Ris, and L. H. Holthuijsen (1999), A third-generation wave model for coastal regions: 1. Model description and validation, *J. Geophys. Res.*, *104*(C4), 7649–7666, doi:10.1029/98JC02622.

Daly, C. J., K. R. Bryan, and C. Winter (2014), Wave energy distribution and morphological development in and around the shadow zone of an embayed beach, *Coastal Eng.*, *93*, 40–54, doi:10.1016/j.coastaleng.2014.08.003.

Daly, C. J., C. Winter, and K. R. Bryan (2015), On the morphological development of embayed beaches, *Geomorphology*, *248*, 252–263, doi:10.1016/j.geomorph.2015.07.040.

Deigaard, R., J. Fredsøe, and I. Hedegaard (1986), Mathematical model for littoral drift, *J. Waterw. Port Coastal Ocean Eng.*, *112*(3), 351–369.

Falqués, A. (2003), On the diffusivity in coastline dynamics, *Geophys. Res. Lett.*, *30*(21), 2119, doi:10.1029/2003GL017760.

Falqués, A., and D. Calvete (2005), Large-scale dynamics of sandy coastlines: Diffusivity and instability, *J. Geophys. Res.*, *110*, C03007, doi:10.1029/2004JC002587.

Fenton, J., and W. McKee (1990), On calculating the lengths of water waves, *Coastal Eng.*, *14*(6), 499–513.

González, M., and R. Medina (2001), On the application of static equilibrium bay formulations to natural and man-made beaches, *Coastal Eng.*, *43*(3–4), 209–225, doi:10.1016/S0378-3839(01)00014-X.

González, M., R. Medina, and M. Losada (2010), On the design of beach nourishment projects using static equilibrium concepts: Application to the spanish coast, *Coastal Eng.*, *57*(2), 227–240, doi:10.1016/j.coastaleng.2009.10.009.

Hanson, H. (1989), Genesis-A generalized shoreline change numerical model, *J. Coastal Res.*, *5*, 1–27.

Hardaway, C. S., and J. R. Gunn (2010), Design and performance of headland bays in chesapeake bay, {USA}, *Coastal Eng.*, *57*(2), 203–212, doi:10.1016/j.coastaleng.2009.10.007.

Harley, M. D., I. L. Turner, A. D. Short, and R. Ranasinghe (2011), A reevaluation of coastal embayment rotation: The dominance of cross-shore versus alongshore sediment transport processes, Collaroy-Narrabeen Beach, southeast Australia, *J. Geophys. Res.*, *116*, F04033, doi:10.1029/2011JF001989.

Hsu, J., and C. Evans (1989), Parabolic bay shapes and applications, *Proc. Inst. Civ. Eng.*, *87*, 557–570.

Hsu, J. R., M. J. Yu, F. C. Lee, and L. Benedet (2010), Static bay beach concept for scientists and engineers: A review, *Coastal Eng.*, *57*(2), 76–91.

Iglesias, G., I. López, R. Carballo, and A. Castro (2009), Headland-bay beach planform and tidal range: A neural network model, *Geomorphology*, *112*(1–2), 135–143.

Kaergaard, K., and J. Fredsoe (2013a), A numerical shoreline model for shorelines with large curvature, *Coastal Eng.*, *74*, 19–32.

Kaergaard, K., and J. Fredsoe (2013b), Numerical modeling of shoreline undulations. Part 1: Constant wave climate, *Coastal Eng.*, *75*, 64–76.

Kaergaard, K., and J. Fredsoe (2013c), Numerical modeling of shoreline undulations. Part 2: Varying wave climate and comparison with observations, *Coastal Eng.*, *75*, 77–90.

Kamphuis, J. W. (1991), Alongshore sediment transport rate, *J. Waterw. Port Coastal Ocean Eng.*, *117*(6), 624–640.

Komar, P. D. (1998), *Beach Processes and Sedimentation*, Prentice-Hall, London.

Komar, P. D., and D. L. Inman (1970), Longshore sand transport on beaches, *J. Geophys. Res.*, *75*(30), 5914–5927.

Kraus, N. C. (1984), Estimate of breaking wave height behind structures, *J. Waterw. Port Coastal Ocean Eng.*, *110*(2), 276–282.

Krumbein, W. C. (1944), *Shore Processes and Beach Characteristics*, U.S. Army Corps of Eng., U.S. Gov. Print. Off., Washington, D. C.

Larsen, L., C. Thomas, M. Eppinga, and T. Coulthard (2014), Exploratory modeling: Extracting causality from complexity, *Eos Trans. AGU*, *95*(32), 285–286, doi:10.1002/2014EO320001.

LeBlond, P. H. (1972), On the formation of spiral beaches, *Coastal Eng. Proc.*, *1*(13), 1331–1343.

LeBlond, P. H. (1979), An explanation of the logarithmic spiral plan shape of headland-bay beaches, *J. Sediment. Res.*, *49*(4), 1093–100.

Limber, P. W., and A. B. Murray (2011), Beach and sea-cliff dynamics as a driver of long-term rocky coastline evolution and stability, *Geology*, *39*(12), 1147–1150.

Limber, P. W., and A. B. Murray (2014), Unraveling the dynamics that scale cross-shore headland relief on rocky coastlines: 2. Model predictions and initial tests, *J. Geophys. Res. Earth Surf.*, *119*, 874–891, doi:10.1002/2013JF002978.

Limber, P. W., A. Brad Murray, P. N. Adams, and E. B. Goldstein (2014), Unraveling the dynamics that scale cross-shore headland relief on rocky coastlines: 1. Model development, *J. Geophys. Res. Earth Surf.*, *119*, 854–873, doi:10.1002/2013JF002950.

Littlewood, R., A. B. Murray, and A. D. Ashton (2007), An alternative explanation for the shape of "log-spiral" bays,paper presented at 6th International Symposium on Coastal Engineering and Science of Coastal Sediment Process '07, pp. 341–350, doi:10.1061/40926(239)26.

Longuet-Higgins, M. S. (1970), Longshore currents generated by obliquely incident sea waves: 1, *J. Geophys. Res.*, *75*(33), 6778–6789, doi:10.1029/JC075i033p06778.

Masselink, G., T. Scott, T. Poate, P. Russell, M. Davidson, and D. Conley (2015), The extreme 2013/14 winter storms: Hydrodynamic forcing and coastal response along the southwest coast of England, *Earth Surf. Processes Landforms*, doi:10.1002/esp.3836, in press.

Mil-Homens, J., R. Ranasinghe, J. S. M. van Thiel de Vries, and M. J. F. Stive (2013), Re-evaluation and improvement of three commonly used bulk longshore sediment transport formulas, *Coastal Eng.*, *75*, 29–39.

Murray, A. B. (2007), Reducing model complexity for explanation and prediction, *Geomorphology*, *90*(3–4), 178–191, doi:10.1016/j.geomorph.2006.10.020. reduced-Complexity Geomorphological Modelling for River and Catchment Management.

Oliveira, F. S., and O. M. Barreiro (2010), Application of empirical models to bay-shaped beaches in Portugal, *Coastal Eng.*, *57*(2), 124–131.

Pelnard-Considere, R. (1956), Essai de theorie de l'evolution des formes de rivage en plages de sable et de galets, in *4th Journees de l'Hydraulique, Les Energies de la Mer*, vol. 3, pp. 289–298. [Available at http://repository.tudelft.nl/view/hydro/uuid:c6e1ce87-23ef-4a3d-86d0-47f3c96518cc/.]

Pilkey, O. H., J. A. G. Cooper, and G. Andrew (2002), Longshore transport volumes: A critical view, *J. Coastal Res.*, *36*, 572–580.

Press, W. H., S. A. Teukolsky, W. T. Vetterling, and B. P. Flannery (1992), *Numerical Recipes in C*, Cambridge Univ. Press, Cambridge, U. K.

Ratliff, K. M., and A. B. Murray (2014), Modes and emergent time scales of embayed beach dynamics, *Geophys. Res. Lett.*, *41*, 7270–7275, doi:10.1002/2014GL061680.

Rea, P. D., and C. C. Komar (1975), Computer simulation models of a hooked beach shoreline configuration, *J. Sediment. Res.*, *45*(4), 866–872.

Silvester, S. K., and R. Ho (1972), Use of crenulate-shaped bays to stabilize coasts, in *Proceedings of the 13th International Conference on Coastal Engineering*, vol. 2, pp. 1347–1365, ASCE, New York, doi:10.9753/icce.v13.%p.

Soulsby, R. L., and J. S. Damgaard (2005), Bedload sediment transport in coastal waters, *Coastal Eng.*, *52*(8), 673–689.

Sunamura, T. (1992), *Geomorphology of Rocky Coasts*, John Wiley, Chichester, New York.

Tanner, W. F. (1958), The equilibrium beach, *Eos Trans. AGU*, *39*, 889–891.

Thomas, T., M. Phillips, A. Williams, and R. Jenkins (2011), Short-term beach rotation, wave climate and the North Atlantic Oscillation (NAO), *Prog. Phys. Geog.*, *35*(3), 333–352, doi:10.1177/0309133310397415.

Turki, I., R. Medina, G. Coco, and M. Gonzalez (2013), An equilibrium model to predict shoreline rotation of pocket beaches, *Mar. Geol.*, *346*, 220–232, doi:10.1016/j.margeo.2013.08.002.

U.S. Army Corps of Engineers (USACE) (1984), *Shore Protection Manual*, US Army Corps of Eng., U.S. Gov. Print. Off., Washington, D. C.

van den Berg, N., A. Falqués, and F. Ribas (2012), Modeling large scale shoreline sand waves under oblique wave incidence, *J. Geophys. Res.*, *117*, F03019, doi:10.1029/2011JF002177.

Van Wellen, E., A. J. Chadwick, and T. Mason (2000), A review and assessment of longshore sediment transport equations for coarse-grained beaches, *Coastal Eng.*, *40*(3), 243–275.

Weesakul, S., T. Rasmeemasmuang, S. Tasaduak, and C. Thaicharoen (2010), Numerical modeling of crenulate bay shapes, *Coastal Eng.*, *57*(2), 184–193.

Yasso, W. E. (1965), Plan geometry of headland-bay beaches, *J. Geol.*, *73*, 702–714.

Zenkovich, V. P. (1967), *Processes of Coastal Development*, Oliver and Boyd, Edinburgh.